Quantification of Fatty Acid Composition Using MRI: Comparison of Accuracy at 1.5, 3 and 7 T.

Lena Trinh

Supervision

Sven Månsson och Pernilla Peterson, Malmö

This work has been conducted at
Medical Radiation Physics, Skåne University Hospital, Malmö

Department of Medical Radiation Physics,
Clinical Sciences, Lund
Lund University

Abstract

The increasing prevalence of obesity and obesity related diseases in this modern world has resulted in a lot of research in the area of water-fat separation with magnetic resonance imaging (MRI). Since the introduction of the two-point Dixon technique, this area of research has expanded and relationships have been discovered between fat content and fatty acid (FA) composition, and diseases such as diabetes and non-alcoholic fatty liver disease.

In this work, an image-based method to quantify fat content and FA composition using MRI has been investigated at three different field strengths (1.5, 3 and 7 T). The aim was to explore the potential advantages associated with increased spectral resolution gained at higher field strengths, such as more accurate estimations of FA composition. The method is based on a concept of describing the FA composition in terms of chain length (*cl*), number of double bonds (*ndb*) and number of methylene interrupted double bonds (*nmidb*), originally published for use in magnetic resonance spectroscopy (MRS).

Both phantom and in vivo experiments were performed. In both studies, MRS measurements were carried out for validation of the method. In addition, values of the FA composition obtained from the Swedish National Food Administration were also used as reference in the phantom study. The in vivo experiment was carried out on subcutaneous adipose tissue in the calf of a volunteer.

Comparing the estimated parameters at all field strength with values obtained from MRS or the values from the Swedish National Food Administration, the accuracy of the estimations seem to increase at higher field strengths. The main drawback of the study was that the acquired images of the phantom at 7 T were not evaluable due to large field inhomogeneity. When comparing the estimations of the FA composition in vivo to the values obtained using MRS, the estimation at 1.5 T was the least accurate and the estimations at 7 T somewhat more accurate than the ones obtained at 3 T. Even though the results indicate better accuracy, additional research is needed to investigate the benefits in using higher field strengths.

Contents

1. Introduction

In recent studies, relationships between fat content in e.g. skeletal muscle and liver, and obesity related diseases such as diabetes and non-alcoholic fatty liver disease have been found [1-3]. Due to the increasing prevalence of obesity, a lot of research has been carried out on fat assessment methods using magnetic resonance imaging (MRI) [4-6]. Although there are other fat quantification methods in use, only MRI offers a non-invasive and non-ionizing imaging method that can quantify fat accumulated in for example subcutaneous and visceral fat, and liver [7].

In 1984, Dixon [4] proposed a method for fat-water separation using MRI, based on the chemical shift between the water and fat signals. By acquiring two images; one where the fat and water signals are in phase and another when the signals are out of phase, a fat and a water image could be obtained by subtraction and addition of the acquired signals, respectively.

One of the fat-water separation methods which was developed from the simple two-point Dixon technique, was introduced by Reeder et al [5] and known as the iterative decomposition of water and fat with echo asymmetry and least-squares estimation (IDEAL). This generalized method estimates different chemical species, such as water and fat, and corrects for the local magnetic offset simultaneously using arbitrary echo times. Yu et al [8] then proposed a modification of the original IDEAL algorithm, T2*-IDEAL, which included a simultaneous estimation of the T_2^* relaxation time. A new, updated version of the T2*-IDEAL technique was later proposed which also included the fact that the fat spectrum consists of several resonances [6] and not only one as assumed in the original IDEAL method.

Not only the fat fraction (*FF*) is of interest. Numerous researchers have suggested a relationship between the fatty acid (FA) composition of skeletal muscle and liver, and different diseases such as diabetes, non-alcoholic fatty liver disease and tumours [1-3, 9]. Estimation of the FA composition may be obtained using magnetic resonance spectroscopy (MRS) where the amplitude of different fat resonances in the acquired spectra are related to the composition of FAs [10]. An example of using MRS as a fat quantification method is in a recent study which the different FA composition of white and brown adipose tissue are examined [11]. Another example of the MRS method is in a study which relates the fraction unsaturated fat to the total visceral fat volume [12].

In the recent publication by Hamilton et al. [13], it was suggested to describe the chemical composition of FAs using the parameters chain length (*cl*), number of double bonds (*ndb*) and number of methylene-interrupted double bonds (*nmidb*). Expressions for each of the relative theoretical fat resonance amplitudes based on these three parameters were also proposed. These parameters can be rewritten to the terms more commonly used when describing FAs: saturated (SFA), monounsaturated (MUFA) and polyunsaturated (PUFA).

Even though MRS has been proven to be a reliable tool for quantification of FA composition [9, 14, 15], the use of an imaging-based quantification tool would also increase the spatial information, which is limited using MRS. This has previously been accomplished by Peterson and Månsson [16], Bydder et al [17] and Berglund et al [18] using the estimation of *cl, ndb*

4

and *nmidb* described by Hamilton et al [13]. Bydder et al. estimated only *ndb*, which was used to calculate *cl* and *nmidb* using experimental relations found in the same work, contrary to Peterson and Månsson which estimated *cl*, *ndb* and *nmidb* independently. Estimating only *ndb* simplifies the fat quantification method and more stable estimations are obtained compared to estimating all parameters. This is, however, based on the assuption that the used expressions describing the relationship between the parameters (*cl* and *ndb*, *nmidb* and *ndb*) are correct for all cases. If estimating all parameters, no such assumptions are needed.

The use of higher field strengths have the advantage of a larger chemical shift and signal-to-noise-ratio (SNR) compared to using lower field strengths. As discussed above, it is because of the chemical shift of the water and the fat signals that these separation and quantification methods work, so because of the higher spectral resolution gained from the larger chemical shift and higher SNR, more accurate estimations of *cl*, *ndb* and *nmidb* may be obtained. This potential gain in accuracy of the estimations of FA composition when increasing the field strength is expected because of the relationships between *cl*, *ndb* and *nmidb*, and the different individual peak amplitudes of the fat spectrum whereas no major gain in the estimation of fat content is expected. This is because of the fact that *FF* depends on the water and total fat signal and not on the individual fat peaks. These improvements of the estimations of FA composition may also affect the image-based quantification method, but in addition, the increase in SNR could be used to obtain higher spatial resolution.

There are, however, some problems which worsen with increasing field strength. The methods described earlier are more or less dependent on good field homogeneity which is harder to obtain at higher field strengths. With increasing field strength, the phase evolution between fat and water is also sampled less frequently which could introduce potential problems with the fat quantification method.

Another way of obtaining higher SNR is by using a larger flip angle. However, this introduces a T_1 relaxation time effect which might not be insignificant. This T_1 bias occurs because of the different T_1 relaxation times of water and fat, and could result in incorrect estimations of the fat content and FA composition. Consequently, it is of interest to minimize T_1 bias as much as possible. This can be achieved, for example, by using a long repetition time (TR) or a small flip angle.

2. Purpose

The purpose of this thesis is to compare the method of simultaneous quantification of fat content and FA composition using MRI at three different magnetic field strengths (1.5, 3 and 7 T) as an in vivo study of the subcutaneous fat of a volunteer and a phantom study. The phantom is constructed using twelve vials containing four different oils with a range of fat contents and FA compositions. The methods dependence on number of reconstructed echoes, flip angle and matrix size is evaluated briefly. For reference, the fat content and FA composition were quantified also using localized spectroscopy.

3. Theory

3.1 FAT SPECTRUM/THE TRIGLYCERIDE MOLECULE

A triglyceride fat molecule consists of three FA chains connected to one glycerol molecule. The chemical structure of these FAs can be described using three parameters: *cl*, *ndb* and *nmidb* following Hamilton et al [13]. By acquiring a spectrum as seen in Figure 1 and obtaining the relative amplitudes of each fat peak, these parameters can be calculated using the expressions shown in Table 1. An example triglyceride molecule and how the FA structure is related to the fat spectrum are also shown in Figure 1.

Table 1 The chemical shifts and relative amplitudes of the different resonances in the fat spectrum from a triglyceride, as described by Hamilton [13].

Peak	Chemical shift (ppm)	Type	Relative amplitude α	Assignment
A	5.39	Olefin	2ndb	-CH=CH-
B	5.29	Glycerol	1	-CH-O-CO-
Water	-	-	-	H_2O
C D	4.20	Glycerol	4	$-CH_2$-O-CO-
E	2.75	Diacyl	2nmidb	$-CH=CH-CH_2-$ CH=CH-
F	2.24	a-Carboxyl	6	$-CO-CH_2-CH_2-$
G	2.02	a-Olefin	4(ndb-nmidb)	$-CH_2-CH=CH-CH_2-$
H	1.6	b-Carboxyl	6	$-CO-CH_2-CH_2-$
I	1.3	Methylene	6(cl-4)-8ndb+2nmidb	$-(CH_2)_n-$
J	0.9	Methyl	9	$-(CH_2)_n-CH_3-$

Depending on *ndb*, the FAs can be saturated (SFA) or unsaturated (MUFA, PUFA). SFA does not have any double bonds at all while MUFA and PUFA have one or more double bonds, respectively. The more common measures of FA composition are the fraction saturated, f_{SFA}, and unsaturaded fat, $f_{MUFA} + f_{PUFA}$, which may easily be calculated using *ndb* and *nmidb* obtained from the methods described in this thesis. By acquiring MR images or spectrums, f_{SFA}, f_{MUFA} and f_{PUFA} can therefore be calculated using equations $(3.1) - (3.3)$ [10, 13, 16]. The total fraction of unsaturated FAs is given by:

$$f_{MUFA} + f_{PUFA} = \frac{\alpha_G}{2 \cdot \alpha_F} = \frac{ndb - nmidb}{3} \qquad (3.1)$$

where α_m denotes the amplitude of fat peak m. This expression is obtained given the fact that all unsaturated fatty acids include two α-olefinic groups (α_G) independent of unsaturation degree, and that α-carboxyl (α_F) is distributed equally among all FAs in the triglyceride.

The amplitude of the diacyl peak (α_E) is directly proportional to the number of methylene hydrogen atoms located between two double bonds which results in the following expression:

$$f_{PUFA} = \frac{\alpha_E}{\alpha_F} = \frac{nmidb}{3} \tag{3.2}$$

with the assumption that the highest unsaturation degree is two (diunsaturation) and α_F is, again, used as a reference. The saturation fraction can then be calculated through

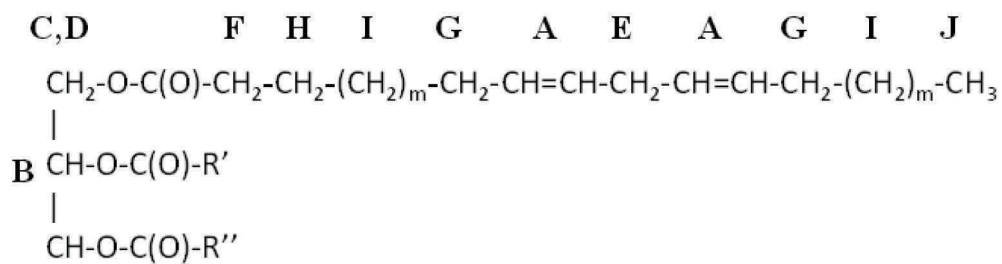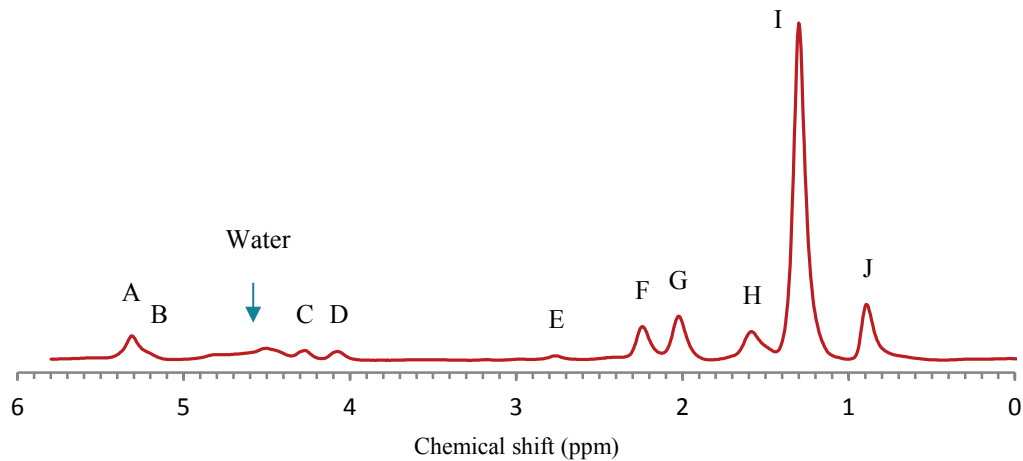$$f_{SFA} = 1 - (f_{MUFA} + f_{PUFA}) \tag{3.3}$$

Figure 1 Spectrum acquired in subcutaneous adipose tissue at 7 T and an example of a triglyceride molecule with the corresponding peak contributions [19].

3.2 SIGNAL MODEL

Assuming that only water and fat contribute to the measured signal from a given voxel, the original gradient echo signal model for water/fat separation may be written as:

$$S(t) = \left(We^{-R_{2,w} \cdot t} + Fe^{-(R_{2,F} - i\omega_F)t}\right)e^{i2\pi\psi t}e^{-R_2^* t} \qquad (3.4)$$

where W and F are the amplitudes of water and fat, respectively. $R_{2,W}$ is the R_2 relaxation rate of water, $R_{2,F}$ is the R_2 relaxation rate of fat, ω is the angular frequency of fat relative to water, ψ is the frequency offset caused by B_0 inhomogeneities and R_2^* is the relaxation rate due to B_0 inhomogeneities. The angular frequency of water is assumed to be zero.

Equation (3.4) above assumes only one fat peak which means that the model does not represent the true fat contribution to the signal. When considering all spectral fat peaks and using the complex field map introduced by Yu et al [8] $\hat{\psi} = i2\pi\psi - R_2^*$ the following signal model is obtained:

$$S(t) = (We^{\sigma_w t} + Ff\sum_{m=1}^{M}\alpha_m e^{\sigma_m t})e^{i\hat{\psi}t} \qquad (3.5)$$

where $\sigma_W = -R_{2,w}$, $\sigma_m = -(R_{2,m} - i\omega_m)$ and α_m is the relative amplitude of the mth fat peak which is obtained from Table 1. Note that each fat peak has individual T_2 relaxation times and phase angles. The normalization factor $f = (6cl - 2ndb + 2)^{-1}$ is defined from Table 1 as the sum of all α_m.

By inserting the expression of α_m given in Table 1, equation (3.5) can be rewritten and expressed in matrix form for N echoes:

$$S_{Nx1} = \Psi AP \qquad (3.6)$$

where

$$\Psi_{NxN} = \begin{bmatrix} e^{i\hat{\psi}t_1} & 0 & \cdots & 0 \\ 0 & e^{i\hat{\psi}t_2} & \cdots & 0 \\ \vdots & \vdots & \ddots & \vdots \\ 0 & 0 & \cdots e^{i\hat{\psi}t_N} \end{bmatrix},$$

$$A_{Nx5} = \begin{bmatrix} e^{\sigma_w t_1} & a_1(t_1) & a_2(t_1) & a_3(t_1) & a_4(t_1) \\ \vdots & \vdots & \vdots & \vdots & \vdots \\ e^{\sigma_w t_N} & a_1(t_N) & a_2(t_N) & a_3(t_N) & a_4(t_N) \end{bmatrix}$$

and

$$P_{5x1} = \begin{bmatrix} W \\ Ff \\ Ff \cdot ndb \\ Ff \cdot nmidb \\ Ff \cdot cl \end{bmatrix}.$$

In A_{Nx5} the following expressions are used for simplification:

$$a_1(t) = e^{\sigma_{AB}t} + 4e^{\sigma_{CD}t} + 6e^{\sigma_F t} + 6e^{\sigma_H t} - 24e^{\sigma_I t} + 9e^{\sigma_J t}$$

$$a_2(t) = 2e^{\sigma_{AB}t} + 4e^{\sigma_G t} - 8e^{\sigma_I t}$$

$$a_3(t) = 2e^{\sigma_E t} - 4e^{\sigma_G t} + 2e^{\sigma_I t}$$

$$a_4(t) = 6e^{\sigma_I t}.$$

These expressions follow from Table 1 and the relations between the amplitudes of the different fat peaks.

3.3 IMAGE RECONSTRUCTION

With A known and N echoes, the collected signals can be expressed as equation (3.6) and the following steps can be used for estimation of FF, fatty acid composition and $\hat{\psi}$ [5, 6, 8]:

1. Starting with a first estimate of the complex field map $\hat{\psi}_0$, a first estimation of the vector P can be obtained with a least-squares inversion:

$$\tilde{P} = (A^T A)^{-1} \cdot A^T \cdot \Psi(-\hat{\psi}_0) \cdot S \tag{3.7}$$

where A^T is the complex conjugate transpose of A and $\Psi(\hat{\psi}_0) \cdot \Psi(-\hat{\psi}_0) = \Psi(-\hat{\psi}_0) \cdot \Psi(\hat{\psi}_0) = \mathbf{I}$ if $\mathbf{I}$ is the identity matrix.

2. The error of $\hat{\psi}_0$ can then be calculated by approximating equation (3.6) with the first order Taylor expansion:

$$S \approx \tilde{\Psi} A \tilde{P} + \tilde{\Psi} \tilde{B} \cdot \begin{bmatrix} \Delta\hat{\psi} \\ \Delta W \\ \Delta Ff \\ \Delta(Ff \cdot ndb) \\ \Delta(Ff \cdot nmidb) \\ \Delta(Ff \cdot cl) \end{bmatrix} \tag{3.8}$$

with

$$
\widetilde{\mathbf{B}} = \begin{bmatrix}
\left(\widetilde{W} \cdot e^{\sigma_w t_1} + \widetilde{Ff} \cdot \sum_{m=1}^{M} \alpha_m e^{\sigma_m t_1}\right) \cdot i2\pi t_1 & e^{\sigma_w t_1} & a_{1,1} & \cdots & a_{1,4} \\
\left(\widetilde{W} \cdot e^{\sigma_w t_2} + \widetilde{Ff} \cdot \sum_{m=1}^{M} \alpha_m e^{\sigma_m t_2}\right) \cdot i2\pi t_2 & e^{\sigma_w t_2} & a_{2,1} & \cdots & a_{2,4} \\
\vdots & \vdots & \vdots & & \vdots \\
\left(\widetilde{W} \cdot e^{\sigma_w t_N} + \widetilde{Ff} \cdot \sum_{m=1}^{M} \alpha_m e^{\sigma_m t_N}\right) \cdot i2\pi t_N & e^{\sigma_w t_N} & a_{N,1} & \cdots & a_{N,4}
\end{bmatrix}
$$

where $a_{n,j} = a_j(t_n)$, $n = 1,\ldots,$N and $j = 1,\ldots,4$.

3. By using least-squares inversion, the error terms can be obtained as follows:

$$
\begin{bmatrix}
\Delta\hat{\psi} \\
\Delta W \\
\Delta Ff \\
\Delta(Ff \cdot ndb) \\
\Delta(Ff \cdot nmidb) \\
\Delta(Ff \cdot cl)
\end{bmatrix} = (\boldsymbol{B}^T\boldsymbol{B})^{-1} \cdot \boldsymbol{B}^T \cdot \left(\boldsymbol{\Psi}(-\hat{\psi}_0) \cdot \boldsymbol{S} - \boldsymbol{A} \cdot \widetilde{\mathbf{P}}\right) \qquad (3.9)
$$

4. A new estimate of $\hat{\psi}$ can now be calculated: $\hat{\psi} = \hat{\psi}_0 + \Delta\hat{\psi}$, which is used to recalculate a new estimation of $\widetilde{\mathbf{P}}$ (Step 1).

The steps above are repeated until $\Delta\hat{\psi}$ becomes smaller than a predefined value or when the maximum number of iterations have been reached. A low-pass filter is then used on the final map of $\hat{\psi}$ for reduction of noise before recalculation of the final estimate of $\boldsymbol{P}$. The estimation requires a priori knowledge of the peak angle σ_m and T$_2$ relaxation time $T_{2,m}$ which may be obtained from e.g. spectroscopy measurements.

3.4 CALCULATION OF FF, FA PARAMETERS AND SATURATION AND UNSATURATION FRACTION

With all elements in $\boldsymbol{P}$ known, *ndb*, *nmidb* and *cl* can be calculated by dividing the last three elements of $\boldsymbol{P}$ with *Ff*. When *ndb*, *nmidb* and *cl* are determined, *f* can be calculated and thus also *F*. The fat fraction (*FF*) can now be calculated as follows:

$$
FF = \frac{F}{F + W} \qquad (3.10)
$$

Using equations $(3.1) - (3.3)$, f_{SFA}, f_{MUFA} and f_{PUFA} can be determined.

In a recent publication by Bydder et al [17], empirical relations of *cl* and *nmidb* are described. These functions were obtained by plotting measured *cl* and *nmidb* against *ndb* of twenty different fat and oils and human fat (marrow, subcutaneous and liver fat) obtained at 3 T, and fitting a linear and a quadric trend line to the data, respectively. The following heuristic expressions were then found: $cl = 16.8 + 0.25 \cdot ndb$ and $nmidb = 0.093 \cdot ndb^2$. These expressions may be used to estimate *cl* and *nmidb* indirectly using *ndb* which could result in a more robust algorithm.

4. Methods

Spectroscopy and imaging were carried out on a phantom consisting of twelve vials with different *FF* and FA compositions and on subcutaneous fat of a volunteer using three different field strengths: 1.5, 3 (Intera, Philips Medical Systems) and 7 T (Acheiva, Philips Medical Systems). The same volunteer was imaged at approximately the same anatomical location at all field strengths. The quantities *FF*, *cl*, *ndb* and *nmidb* were calculated, using both imaging and spectroscopy data, in all phantom and in vivo acquisitions. Spectroscopy measurements were also used for determination of a fat signal model (chemical shifts and T_2 relaxation times of each signal component) needed for imaging.

4.1 PHANTOM CONSTRUCTION

A phantom consisting of twelve vials was made using four different oils: coconut, palm, soybean and grape seed. The oils were chosen to create a wide span of *cl*, *ndb* and *nmidb* in the phantom. Each of the oil types were made into three vials with different fat contents: 100, 30 and 10 percent by weight (Figure 2).The pure oils were poured into the vials without adding anything, although the coconut and palm oils had to be melted before being poured into the vials. The vials containing 30 and 10 percent fat were mixed with an emulsifier (sodium dodecyl sulfate, Sigma Aldrich) and agarose (Lonza) to create stabile and homogeneous emulsions. Nickel nitrate was added to shorten the T1 relaxation times and therefore reducing bias from T1 relaxation.

The phantom was put in a water bath while performing imaging and spectroscopy to obtain better field homogeneity and therefore facilitate the shimming procedure.

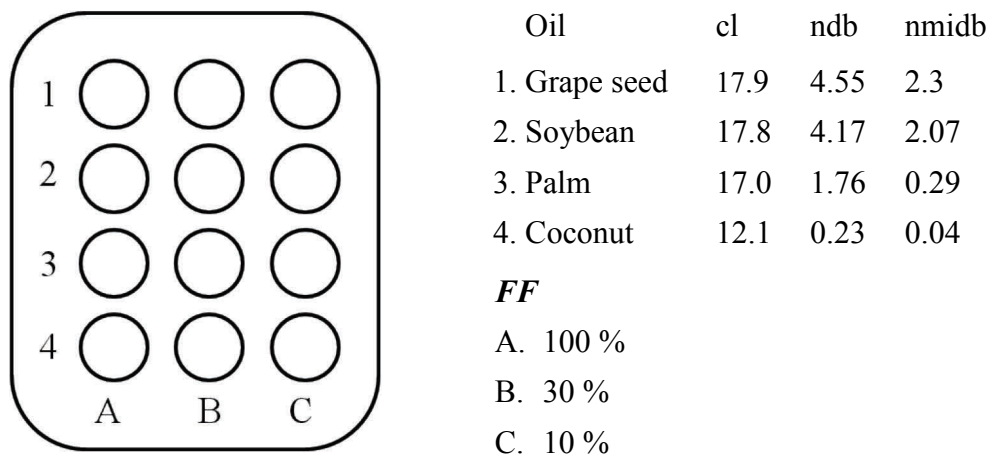| Oil	cl	ndb	nmidb
1. Grape seed	17.9	4.55	2.3
2. Soybean	17.8	4.17	2.07
3. Palm	17.0	1.76	0.29
4. Coconut	12.1	0.23	0.04

FF

A. 100 %

B. 30 %

C. 10 %

Figure 2 Schematic figure of the phantom construction with the different oil types, their parameter values and the fat fraction in each vial. The reference parameters (*cl*, *ndb* and *nmidb*) are calculated from data obtained from the Swedish National Food Administration.

4.2 PHANTOM IMAGING

To investigate the possibility of acquiring images with higher spatial resolution than what was used in the earlier work by Peterson et al. [16], images with two different matrix sizes were acquired (64x64 and 96x96). In addition to using a small flip angle to reduce the T_1 effects in the estimations, a larger flip angle was used to obtain a higher SNR and thus perhaps a more accurate estimation of the FA composition even if a T_1 bias is introduced. Accordingly, for all field strengths, three acquisitions were made with two different matrix sizes and two flip angles: 64x64 matrix with flip angle 8°, 64x64 matrix with 80° and 96x96 matrix with 80°.

Apart from the matrix size and flip angle, the following parameters were used for all acquisitions: repetition time (TR) 600 ms, number of signal averages (NSA) 8, Field of view (FOV) 128x128 mm^2, slice thickness 5 mm and number of echoes 32. Different first echo times (TE_1) and inter echo times (ΔTE) were used depending on field strength, matrix size and flip angle (Table 2). The bandwidth was different for the three field strengths: 2500, 2010 and 3906 Hz/pixel for 1.5, 3 and 7 T respectively.

The SENSE-Head-6 coil was used for the 1.5 T acquisitions, the SENSE-Head-8 coil was used for the acquisition made with the 3 T scanner and a dual coil was used for the 7 T scanner.

At 1.5 and 3 T, the vials were placed upright and a coronal slice through the mid of the vials was acquired. Due to shimming difficulties, a different phantom set up was used at the 7 T scanner. The vials were placed in a horizontal position and an axial slice was acquired.

Table 2 Parameters for the imaging experiments: flip angle, TE_1 and ΔTE for each field strength and matrix size respectively.

Field strength (T)	Matrix size	Flip angle (degrees)	TE_1 (ms)	ΔTE (ms)
1.5	64x64	8	2.0	1.8
	64x64	80	2.1	1.8
	96x96	80	2.4	2.2
3	64x64	8	1.58	1.35
	64x64	80	1.68	1.35
	96x96	80	1.87	1.53
7	64x64	8	1.82	1.53
	64x64	80	1.82	1.53
	96x96	80	1.78 (1.82 in vivo)	1.53

4.3 IN VIVO IMAGING

A transversal slice under the right knee of the volunteer was chosen. The same imaging parameters and set ups as for the phantom imaging were used except for the coils (Table 2). The 1.5 and 3 T acquisitions were made using a SENSE-flex-L coil and for the 7 T acquisitions a Small-Animal-Tx/Rx was used. The number of echoes collected was 32 for all acquisitions.

4.4 IMAGE RECONSTRUCTION AND ANALYSIS

All imaging data was evaluated and reconstructed, and *FF*, *cl*, *ndb* and *nmidb* calculated in every voxel, using MATLAB and the iterative procedure described earlier (3.3 *Image reconstruction*). To avoid eddy current-related phase errors of the first echo [20], the phase information was replaced in each iteration by an estimated phase, $\angle\left(\hat{S}(TE_1)\right)$ where $\angle$ denotes the angle, using equation (3.5) and the phases of the following echoes.

The peak information needed for the reconstruction (chemical shifts and T_2 relaxation times) was obtained from the spectrum analysis. The chemical shift of each peak and acquisition was weighted by the peak amplitude before averaging over all the vials to obtain a single chemical shift for each fat resonance.

The acquisitions using matrix size 64x64 and flip angle 8° were used for all analysis except when evaluating the methods dependence on the matrix size and flip angle.

Although 32 echoes were collected in each acquisition, only 20 echoes were used for reconstruction except when evaluating the dependence of the reconstruction algorithm on the number of echoes. Then 10, 16, 22 and 32 echoes were used.

Using MATLAB, regions-of-interest (ROIs) were chosen in the center of every vial for all reconstructed images of the phantom. In the in vivo images, the ROI was placed approximately in the same area as the spectroscopy voxel (Figure 3). The average value of each ROI in the phantom was plotted against the corresponding value obtained from the Swedish National Food Administration. The average value in each ROI in vivo was plotted against the corresponding MRS values in the same manner.

To investigate any possible relations between the calculated *ndb* values and the *cl* or *nmidb* values (cf. the empirical relations found using data acquired at 3 T by Bydder et al.), the *cl* and *nmidb* values from each in vivo image voxel were plotted against the corresponding *ndb* value.

4.5 SPECTROSCOPY

All spectroscopy measurements were performed in the same session as the imaging acquisitions, and therefore with the same set up and coils, and acquired with a stimulated echo acquisition mode (STEAM) localized spectroscopy. The position of the in vivo spectroscopy voxel was chosen according to Figure 3 and was approximately the same for all scanners. The phantom spectroscopy voxel was placed in the center of each vial to minimize artifact influences.

Two spectroscopy sequences were acquired in every vial. In the first sequence, five echo times (10, 20, 30, 50 and 80 ms) were acquired in order to estimate the T_2 relaxation times. In the second sequence, one echo time (10 ms) was acquired but with longer TR (5000 ms) compared to the first sequence (TR 2000 ms), to reduce T_1 bias. The shortest TE for the in vivo 7 T acquisitions was 12 ms (minimum for the chosen in vivo settings) instead of 10 ms. NSA was set to 16 for all acquisitions.

The mixing time (TM) was always set to the shortest possible value which varied between the field strengths and voxel sizes. Also, a different bandwidth was used to avoid folding of the spectrum depending on the field strength (Table 3).
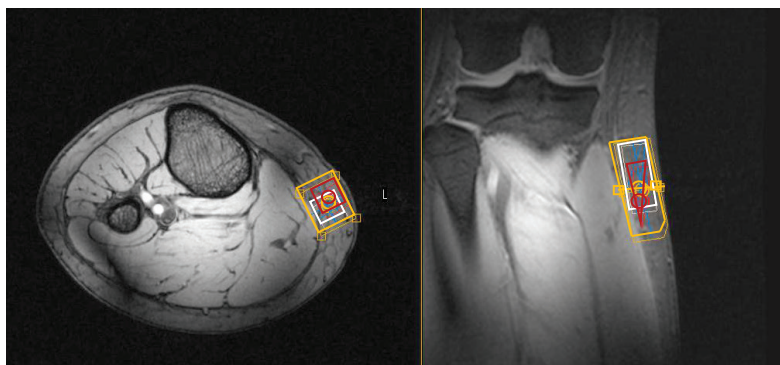

Figure 3 Placement of the fat and water spectroscopy voxel (red and white, respectively) and shim box (yellow) in vivo.

Table 3 Voxel size, BW and TM for the STEAM spectroscopy acquisitions.

Field strength (T)		Voxel size (cm^3)	BW (Hz)	TM (ms)
1.5	Phantom	20x10x10	2000	11
	In vivo	12x8x20	2000	12
3	Phantom	20x10x10	2000	15
	In vivo	12x8x20	2000	15
7	Phantom	10x10x10	4000	14
	In vivo	30x10x10	4000	14

4.6 SPECTRUM ANALYSIS

All acquired spectrums were analyzed using the AMARES algorithm included in the jMRUI (v.5) software package. One or several Gaussians were fitted to each detectable peak amplitude and frequency. Soft constraints were used on frequencies and in some cases, the line widths were fixed to the line width of the methylene peak. When needed, some spectrums were corrected for eddy currents using a MATLAB (r2012b, MathWorks) script before estimations were carried out in jMRUI [21, 22].

The T_2 relaxation time of each peak was calculated from the series of multiple echo times by plotting the amplitude of the signal against the echo times (10/12, 20, 30, 50 and 80 ms). Monoexponential curves were then fitted to the data using Office Excel 2007 (Microsoft) and the T_2 relaxation time of each resonance and acquisition was obtained from the fitted exponential function. The T_2 values were weighted by the corresponding R^2 value of the fitted exponential curve before being averaged over all vials to obtain a single T_2 relaxation time per resonance peak. The average T_2 of each resonance was used to calculate the signal amplitudes at $t = 0$ in the spectra acquired with a longer TR.

Using the T_2 corrected peak amplitudes and the peak amplitudes from Table 1, an estimation of *ndb*, *nmidb* and *cl* was carried out in MATLAB. The fat resonances were mainly divided into four groups: Methyl; Metylene and β-Glycerol; α-Olefin and α-Carboxyl; and Diacyl. If the olefinic peak was sufficiently separated from the water peak and detectable, it was included in the estimation resulting in a total of five groups instead. The fat fraction was simply calculated using $FF = \frac{\sum_{m=1}^{M} \alpha'_m}{\alpha'_w + \sum_{m=1}^{M} \alpha'_m}$ where α'_m and α'_w are the T_2 corrected amplitudes of fat peak *m* and the water peak, respectively. This was done for all spectrums acquired in vivo and in phantom.

5. Results

5.1 FAT SIGNAL MODEL

The range and average value of the T_2 relaxations times and chemical shifts of the phantoms obtained from the spectrum analysis are shown in Table 4 below.

Table 4 The average T_2 relaxations times and chemical shifts of the phantoms estimated from the acquired spectrums for all three field strengths. The range of T_2 relaxations times is given in parentheses.

Peak	1.5T T2 (ms)	1.5T Observed chemical shift (ppm)	3T T2 (ms)	3T Observed chemical shift (ppm)	7T T2 (ms)	7T Observed chemical shift (ppm)
A + B	50.4 (31.3 - 100)	5.30	43.0 (25.0 - 125)	5.28	30.1 (22.7 - 52.6)	5.27
Water	49.9 (37.0 - 62.5)	4.82	41.6 (29.4 - 55.6)	4.83	33.3 (19.6 - 41.7)	4.76
C + D	44.7 (19.2 - 76.9)	4.22	29.1 (22.7 - 40.0)	4.19	27.5 (14.1 - 58.8)	4.16
E	41.7 (35.7 - 47.6)	2.74	49.9 (38.5 - 111)	2.76	31.4 (13.5 - 41.7)	2.75
F	31.8 (25.6 - 37.0)	2.25	33.1 (21.7 - 45.5)	2.25	33.4 (20.4 - 50.0)	2.25
G	30.1 (27.0 - 34.5)	2.03	33.7 (21.7 - 55.6)	2.03	28.7 (11.2 - 35.7)	2.03
H	39.3 (28.6 - 55.6)	1.59	38.4 (15.2 - 66.7)	1.59	25.5 (8.55 - 52.6)	1.58
I	59.5 (47.6 - 71.4)	1.30	55.2 (34.5 - 83.3)	1.30	47.7 (27.8 - 90.9)	1.30
J	71.5 (50.0 - 90.9)	0.88	49.0 (29.4 - 55.6)	0.90	50.7 (20.4 - 83.3)	0.90

Figure 4 illustrates some of the acquired spectra; in vivo and 30 % soybean oil. It is evident that a much higher spectral resolution is obtained with higher field strengths when performing spectroscopy in vivo. This advantage is not as evident when comparing the soybean spectrums. This is probably due to shimming problems which is worse for higher field strengths and phantoms compared to lower field strengths and in vivo. This can also be seen in the results of the MRI acquisitions (Figure 5 and Figure 11).
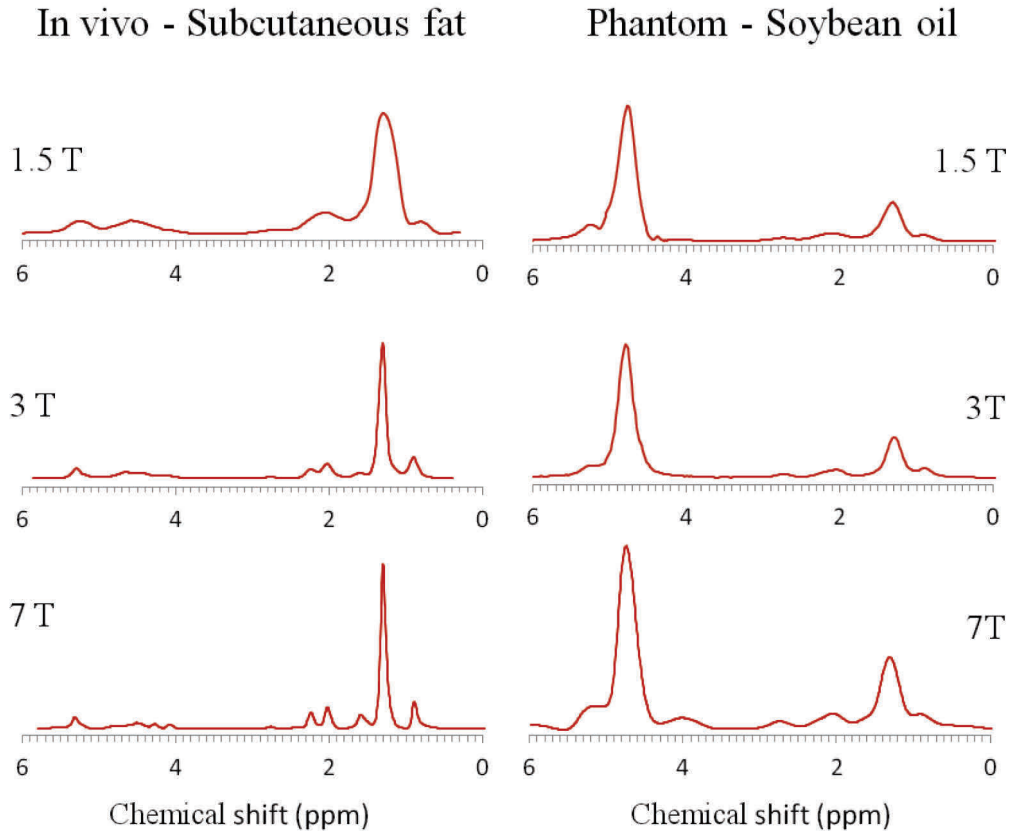
Figure 4 Spectrum acquired at different field strengths. The ones on the left hand side are the spectrums obtained in vivo and the ones on the right hand side are obtained from the 30% soybean vial. The benefit with higher field strengths is much more obvious in vivo than for phantoms. This, however, is probably due to the fact that it is more difficult to get a homogeneous field in vials and for higher field strengths.

5.2 PHANTOM

The reconstructed images from the phantom study using twenty echoes are shown in Figure 5 together with the reconstructed water image and the R_2* image. Due to shimming difficulties and therefore poor images, the phantom images acquired with the 7 T scanner will not be evaluated further in this work. Comparing the vials in the images showing *cl*, *ndb* and *nmidb*, the 3 T scanner seems to produce images where the vials within the same oil type are more similar compared to the 1.5 T scanner. The reconstructed *FF* images do not seem to depend on field strength or fat type as much as the rest of the parameters (*cl*, *ndb* and *nmidb*). The reconstruction algorithm seems to be more robust in the vials with high *FF*. Although true for all field strengths, this is more obvious in the reconstructed images using 1.5 T. The estimations of *cl*, *ndb* and *nmidb* in the vials with lower *FF* are more accurate at 3 T compared to 1.5 T. The artifact visible in the upper part of the phantom is due to worse field inhomogeneity in this part of the image.
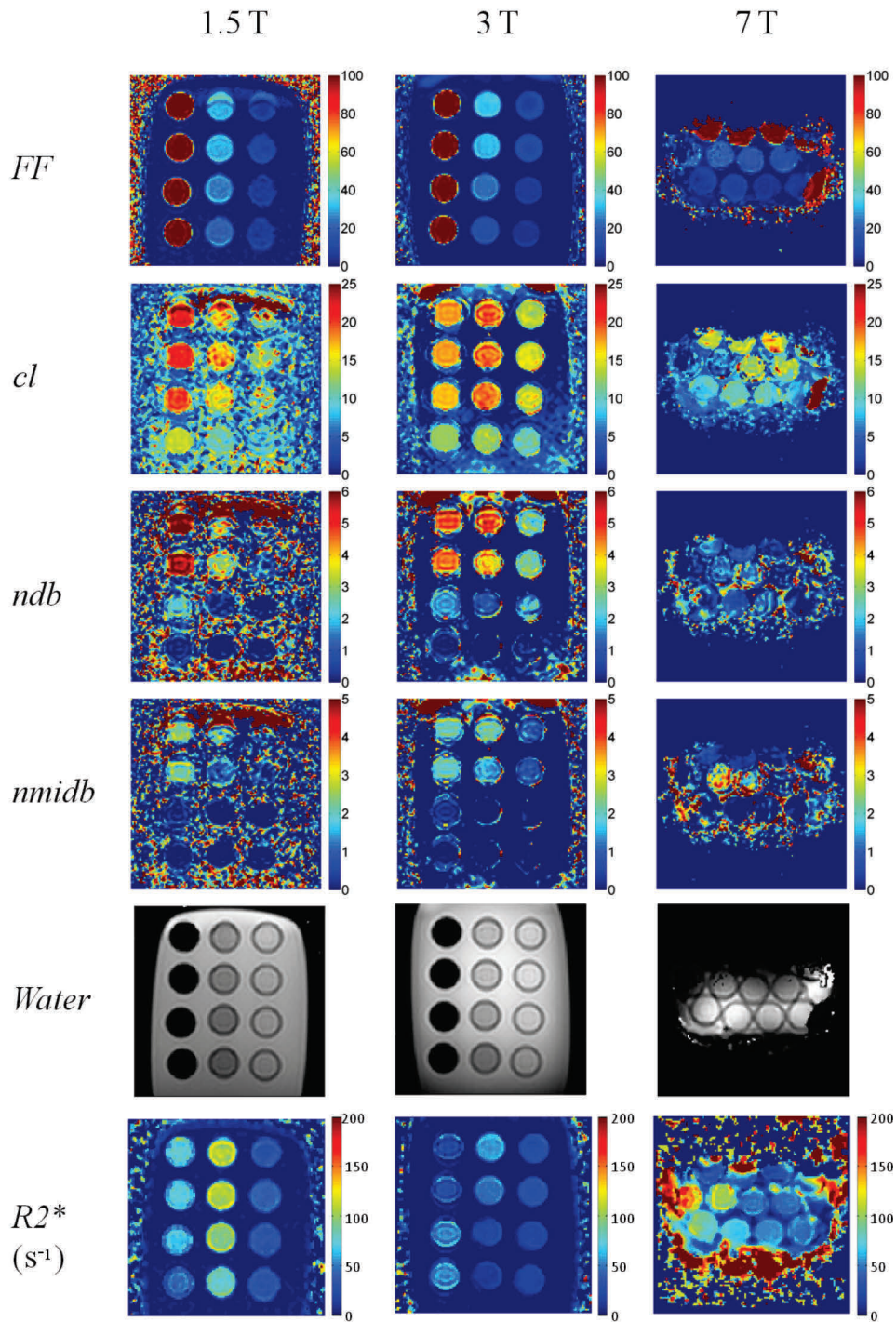
Figure 5 Results obtained from the reconstruction estimating *FF*, *cl*, *ndb* and *nmidb* using three field strengths (1.5, 3 and 7 T), 20 echoes, matrix size 64x64 and flip angle 8°. The reconstructed water image and the R_2* image is also shown for all field strengths. The vials are placed in the same order as in Figure 2 for 1.5 and 3 T. Because of shimming problems, the images acquired with the 7 T scanner will not be investigated further in this report.

In Figure 6 the estimated *FF* values are plotted against the true *FF* values known from the construction of the phantom. The rest of parameters (*cl* , *ndb* and *nmidb*), are plotted against the true values obtained from the Swedish National Food Administration. From these plots, the same results can be concluded as from a visual inspection of the images, but the results are more apparent. It is obvious that the method works better for higher *FF* than lower *FF* as concluded from the images in Figure 5. Comparing the two field strengths in Figure 6, the estimated values from the 3 T images are much closer to the true values except for *FF*, where 1.5 T is slightly more accurate.
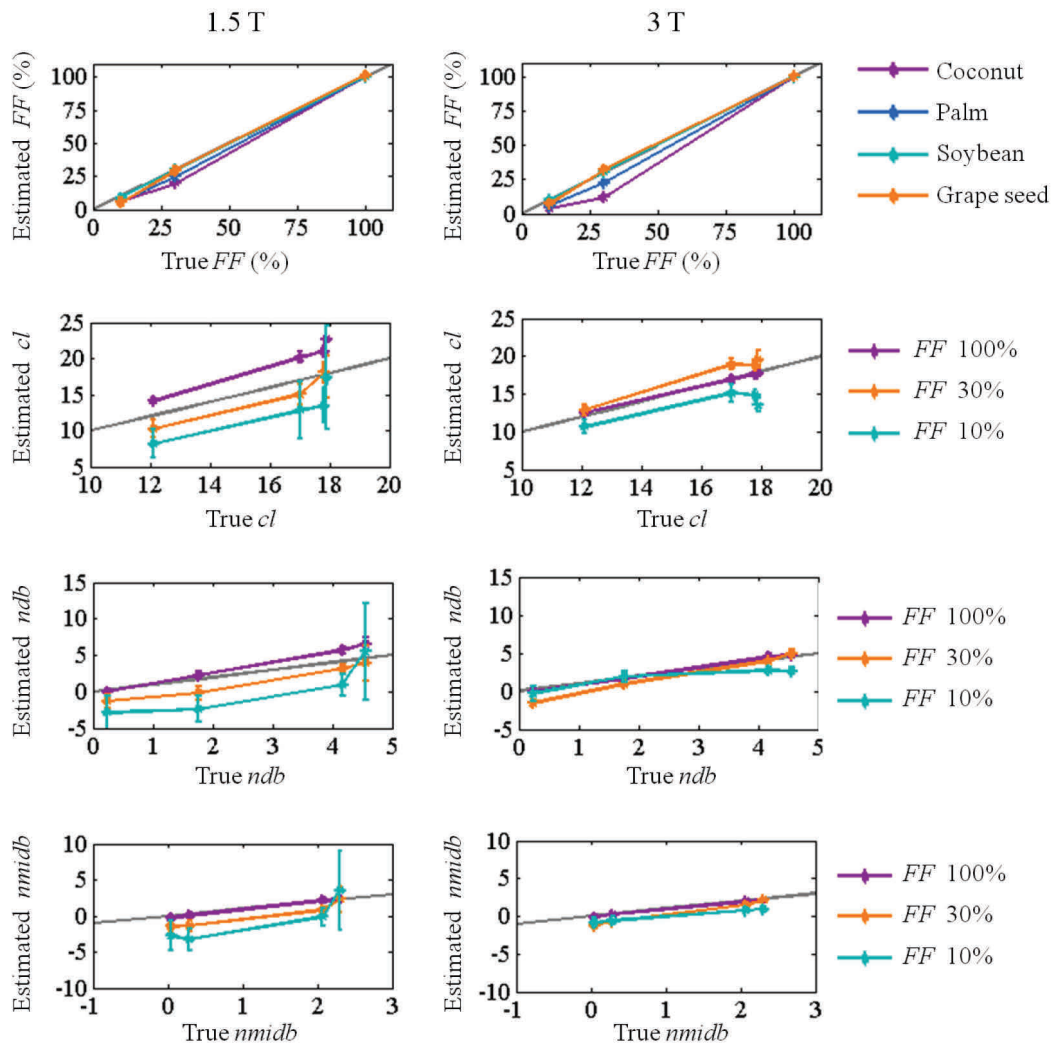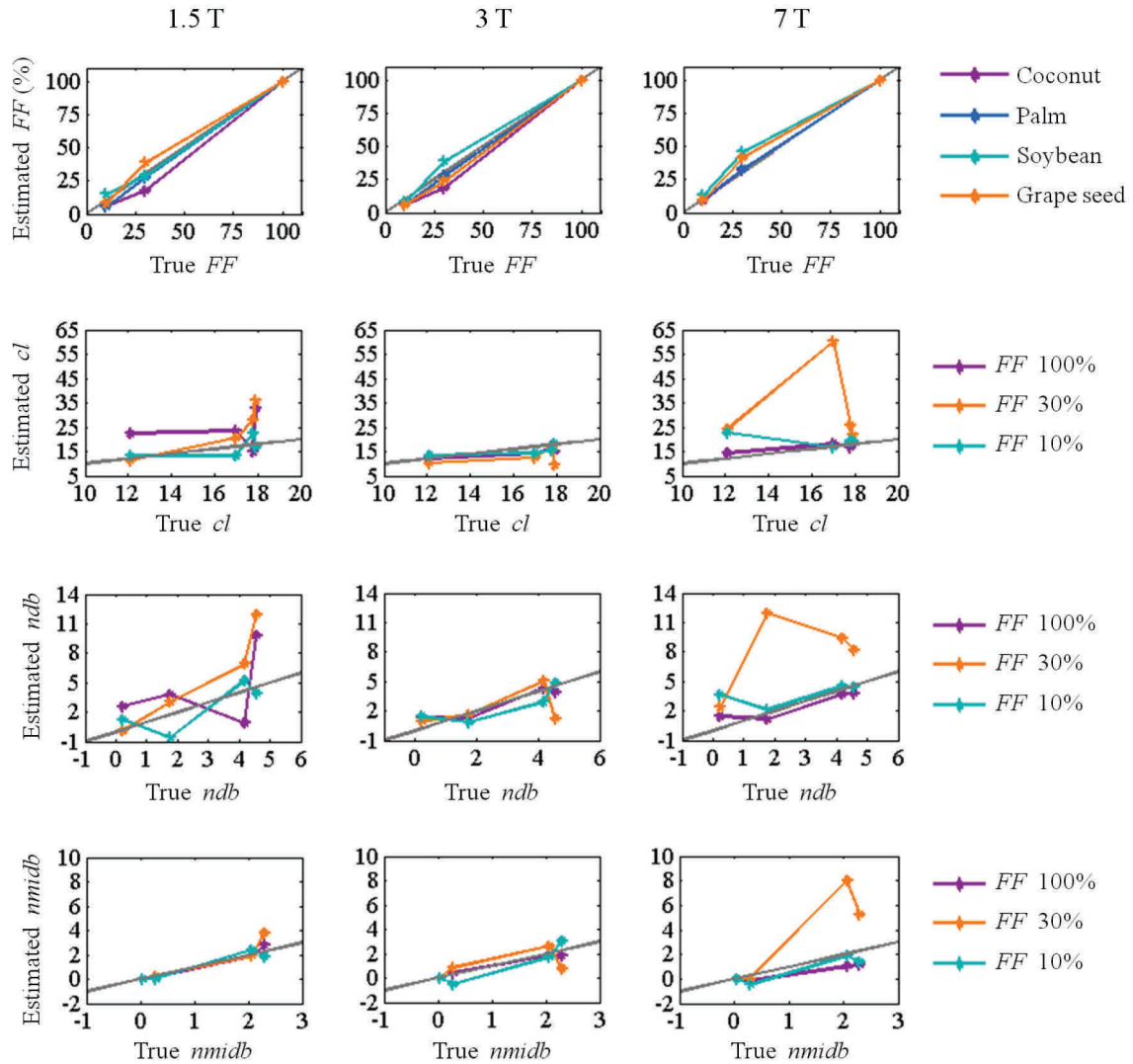

Figure 6 Diagrams comparing the estimated *FF*, *cl*, *ndb* and *nmidb* obtained from MRI with the true values calculated from data obtained from the Swedish National Food Administration. The gray line represents the perfect match between the estimated and true value of *FF*, *cl*, *ndb* and *nmidb*. The more accurate estimations are achieved in pure fat vials and most of the estimations using images acquired from the 3 T scanner is closer to the true values than the 1.5 T images.

In Figure 7 the estimated parameters obtained from the spectroscopy measurements are plotted against the true values obtained from the Swedish National Food Administration. Similar to the imaging estimation, the *FF* estimations are constant through the different field strengths. Except for the estimations in the vials containing *FF* = 30%, the estimations seem more accurate at 3 and 7 T compared to 1.5 T. Comparing these MRS results with the MRI results (Figure 6), the MRI method seems to be at least as accurate as the MRS method.

Figure 7 Diagrams comparing the estimated *FF*, *cl*, *ndb* and *nmidb* obtained from MRS with the true values calculated from data obtained from the Swedish National Food Administration. The gray line represents the perfect match between the estimated and true value of *FF*, *cl*, *ndb* and *nmidb*. The best estimations are achieved in pure fat vials. The estimations in the vials with *FF* = 30% seem to differ the most from the true values.
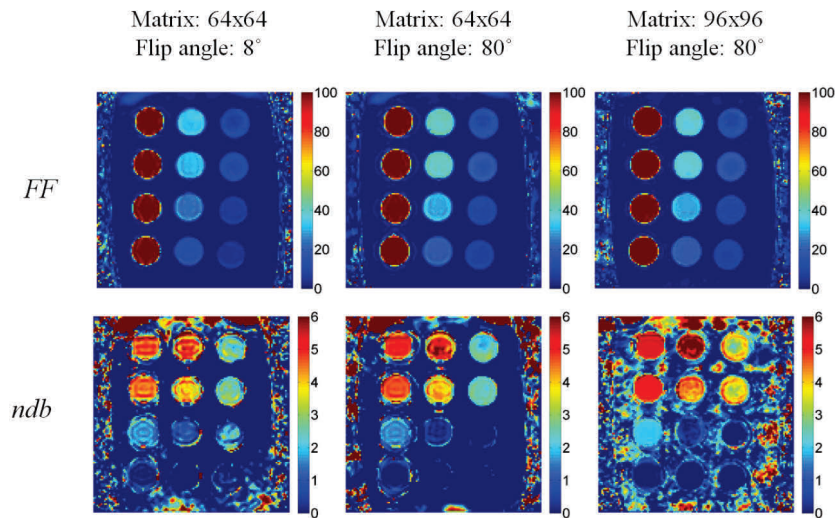
Figure 8 Reconstructed images with different matrix sizes (64x64 and 96x96) and flip angles (8° and 80°) using 3 T. There is an overestimation of *FF* when using 80° compared to 8° but no dependence on matrix size. The estimation of *ndb* seems to depend on both matrix size and flip angle. The most obvious differences between the two matrix sizes are the lower SNR and the less visible ring artifacts in the vials when using the larger matrix size.
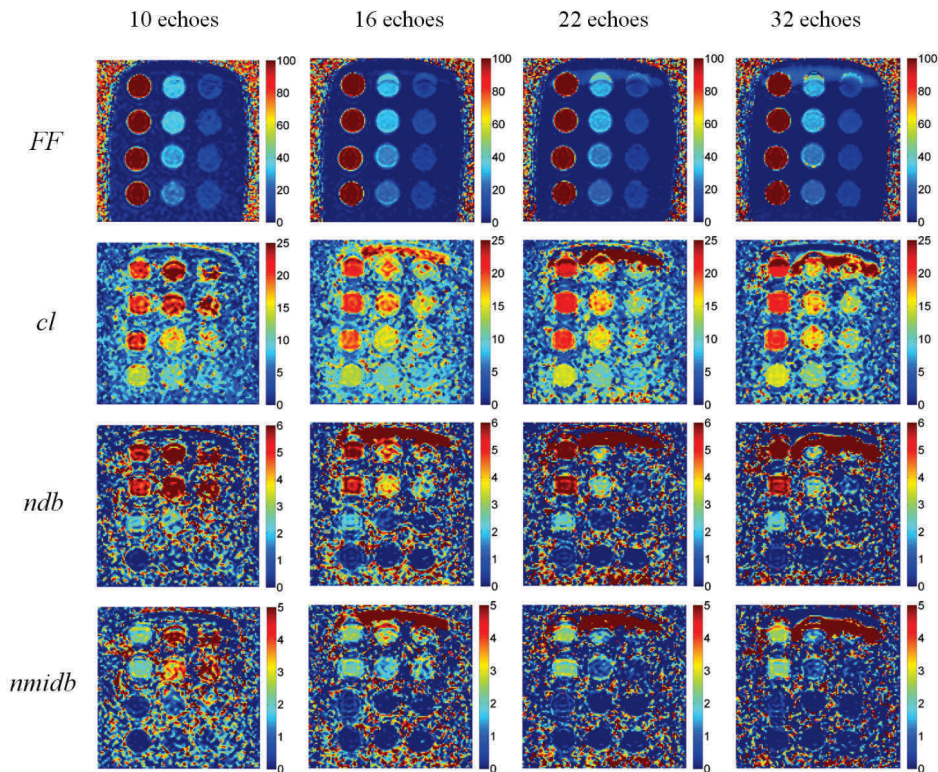
1.5 T

Figure 9 Estimated parameters (*FF*, *cl*, *ndb* and *nmidb*) using different number of echoes (10, 16, 22 and 32) for 1.5 T. The *FF* is relatively constant and independent of number of echoes used in the reconstruction algorithm. The rest of the parameters vary slightly, mostly when using few echoes, but stabilize when using a larger number of echoes. Artifacts in the upper part of the image occur due to field inhomogeneity as the number of echoes increases.

21

The results of the reconstructed images acquired with different flip angles and matrix sizes at 3 T can be seen in Figure 8. The same number of echoes (20) was used for all reconstructions. A slightly higher *FF* is estimated in the images where the larger flip angle is used but the estimation of *ndb* seems to depend more on the matrix size than the flip angle. The noise level is higher when the lower flip angle is used and for the larger matrix size. The signal is also more homogenous in the vials in the images using matrix size 96x96 and the ring artifacts are less visible compared to the images obtained from using the matrix size 64x64.
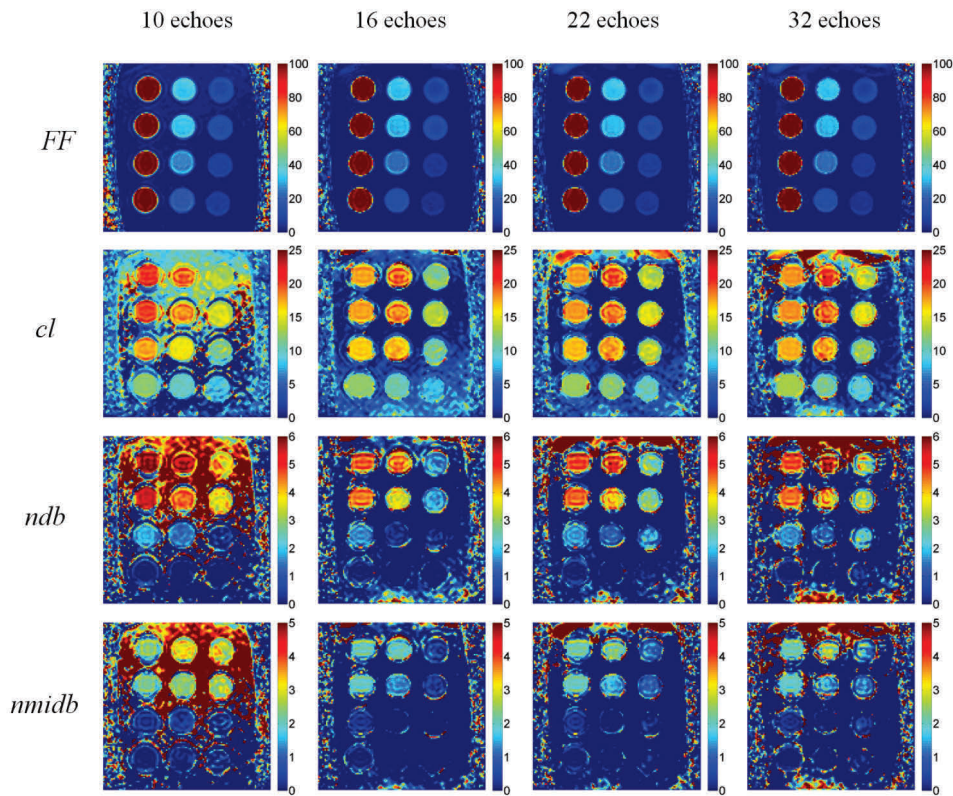

Figure 10 Estimated parameters (*FF*, *cl*, *ndb* and *nmidb*) using different number of echoes (10, 16, 22 and 32) for 3 T. Also for this acquisition, *FF* is relatively constant and independent of number of echoes used in the reconstruction algorithm. The rest of the parameters vary slightly, mostly when using few echoes, but stabilize when using a larger number of echoes. Artifacts in the upper part of the image occur due to field inhomogeneity as the number of echoes increases.

In Figure 9 and Figure 10 the reconstructed images using 10, 16, 22 and 32 echoes are shown for 1.5T and 3T, respectively. The artifacts in the upper part of the images and the lower part of the 3 T images which worsen with number of echoes for both field strengths are due to field inhomogeneities. Comparing the images with fewer echoes with the images reconstructed with a larger number of echoes, the estimated parameters seem more stable when using many echoes. However, the artifacts due to field homogeneity worsen with the number of echoes.
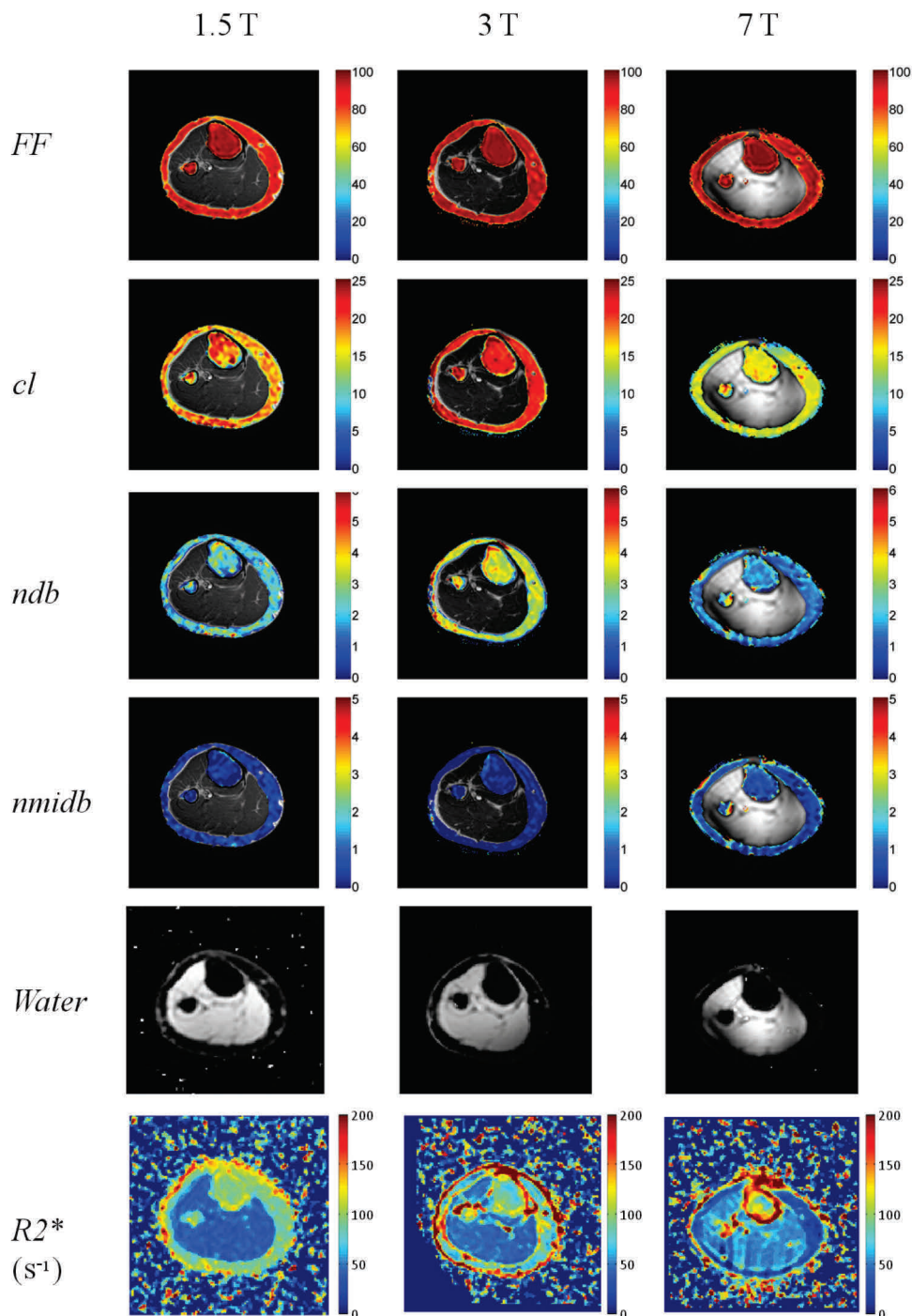
5.3 IN VIVO

Figure 11 Estimated *FF*, *cl*, *ndb* and *nmidb* in vivo using three field strengths (1.5, 3 and 7 T). The reconstruced water image and the R_2* image is also shown for all field strengths. The estimated *FF* seems relatively independent of field strength in the same way as the phantom images. The rest of the parameters, however, do not seem independent of field strength. A comparison between the image values and the values obtained with spectroscopy is made in Figure 12.

The results from the in vivo imaging are shown in Figure 11. A *FF* threshold of 65% was used to exclude data points which are not subcutaneous fat. The estimated images of *FF*, *cl*, *ndb* and *nmidb* are overlaid on anatomic images obtained during the same sessions as the image acquisitions. The *FF* images are quite consistent and do not seem to depend on field strength contrary to *cl* and *ndb* where the parameters vary between the field strengths. Comparing these images only, it is hard to determine which of the field strengths results in more accurate estimations.

Figure 12 compares the values of *FF*, *cl*, *ndb* and *nmidb* obtained from the imaging method with the values obtained with spectroscopy. This comparison makes it easier to evaluate the in vivo results in terms of accuracy. The acquisitions at 7 T seem to match the MRS values better than the acquisitions at 1.5 and 3 T, particularly when estimating *cl* and *ndb*. The assessment of *cl* and *ndb* using spectroscopy at 1.5 T are greatly overestimated. Possible causes of this could be difficulties with the assessment of the fat peak amplitudes and the T_2 relaxation times calculations.
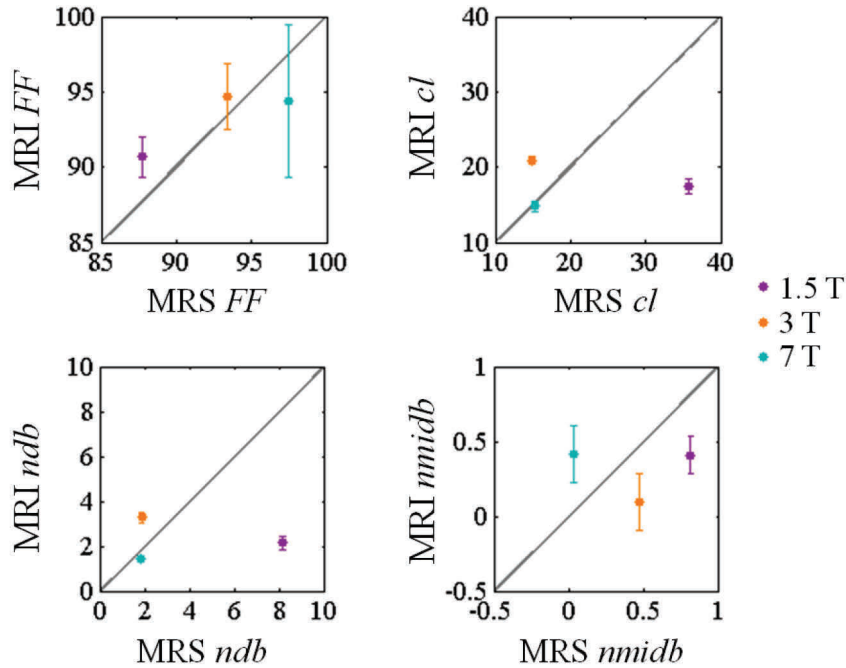

Figure 12 Diagrams comparing the estimated *FF*, *cl*, *ndb* and *nmidb* using MRI with the ones obtained from spectroscopy. The gray line represents the perfect match between the two methods. In these diagrams, the estimations seem to correlate slightly better between MRI and MRS at 7 T. The error bars represents the standard deviation.

In Figure 13, *cl* and *nmidb* is plotted against the corresponding *ndb* in every voxel in the in vivo images excluding the background noise and the voxels with *FF* less than 65% (cf. Figure 11) for all three field strengths. The experimental relations described by Bydder et al [17] using 3 T are included in the diagrams for comparison. The diagrams imply a trend between the parameters (*cl* and *ndb*, *nmidb* and *ndb*) although not perfectly describable by the expressions found by Bydder.
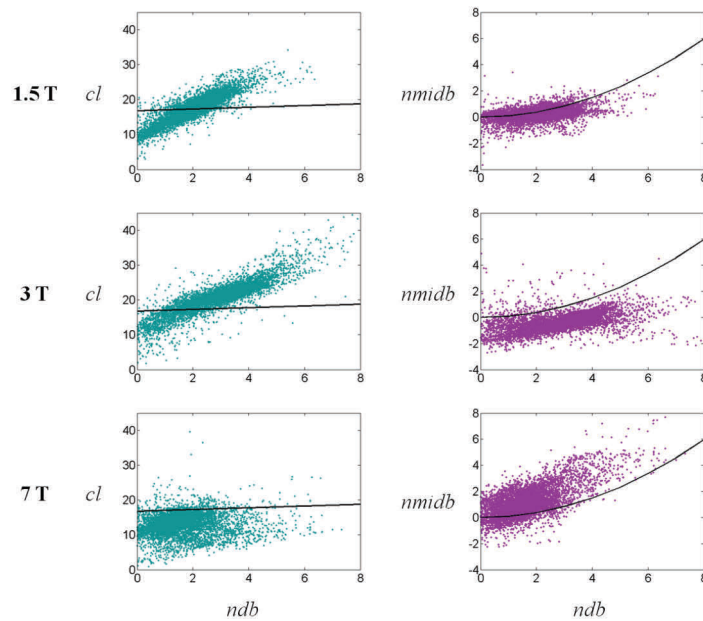
Figure 13 Estimated values of *cl* (turquoise) and *nmidb* (purple) are plotted against *ndb* in every voxel in the reconstructed images excluding background noise and voxels with *FF* less than 65% (see Figure 11). For comparison, the empirical equations obtained using 3 T proposed by Bydder et al [17] are also shown (black). Although not fitted perfectly to Bydder's equations, trends between the parameters are implied.

6. Discussion

In this thesis, quantification of FA composition in phantoms and in vivo has been carried out using MRI at 1.5, 3 and 7 T. The imaging method has been validated with MRS measurements also performed in this work. Although quite modest, improvement can be seen when using higher field strengths. When comparing the estimations of the parameters in the phantom study, vials with lower *FF* could be estimated more accurately using 3 T compared to using 1.5 T (Figure 5 and Figure 6). Although it is hard to compare the field strengths only using the results in Figure 11, comparing the MRI method to the MRS measurements performed in vivo, a slightly better agreement were obtained at 7 T compared to 3 T as shown in Figure 12.

The advantage of using higher field strengths in spectroscopy is more obvious in the in vivo acquisitions comparing to the phantom measurements (Figure 4). It is probably due to shimming problems at higher field strengths that there is no or little improvement when comparing the phantom spectra acquired at different field strengths. Worth noting is also the fact that different voxel sizes had to be used when performing MRS at the different field strengths. This introduces a bias; however, all spectra seemed to have good SNR when evaluating them. In future works, the same voxel size should be used to avoid this source of bias.

Unfortunately, the reconstructed phantom images at 7 T were not evaluable because of large field inhomogeneities. A different phantom construction and set up should be considered in the future to minimize shimming difficulties.

Using a larger matrix size clearly improves the reconstructed images in terms of ring artifacts, which is less apparent in the images using matrix size 96x96 compared to using matrix size 64x64 as can be seen in Figure 8. Although the calculation of *FF* seems independent of matrix size, it is overestimated when using a larger flip angle. The calculation of *ndb* seems to be dependent on both flip angle and matrix size, where the dependence of matrix size is more evident. Compared to the true values of *ndb*, the estimated values using the smaller flip angle is more accurate than the estimation using the larger flip angle. This is probably because of the T_1 bias introduced when using a larger flip angle. In other words, no gain in using a larger flip angle was found in this study. However, the method's dependence on these variables needs to be explored further.

The investigation of the method's dependence on number of echoes showed some dependence mainly when using few echoes. When choosing the number of echoes to use in the reconstruction in the future, one should choose a number of echoes which results in a stable reconstruction but still avoids the effects of field homogeneity. In this study the optimal number of echoes was approximately twenty. In this work, the choice of number of acquired echoes and the used ΔTE were based on the work by Berglund et al. [18]. It should be noted that the same number of echoes do not correspond to the same phase evolution sampling at different field strengths.

Estimations of *cl*/*ndb*/*nmidb* made in previous in vivo studies have presented rather consistent results. In a spectroscopy study, the FA composition in calf subcutaneous tissue was measured in twenty healthy volunteers at 7 T which resulted in 17.5/2.89/0.7 [19]. Another work presented 17.5/1.92/0.82 obtained from spectroscopy measurements on the liver [13]. Estimations from imaging methods have also been presented: 18.4/1.92/0.4 in subcutaneous fat from the thigh of a volunteer [16] and an average of 20.3/2.73/0.6 from three different locations in subcutaneous adipose tissue of a thigh [18]. Comparing the results from this work with those presented from previous works, the parameters are both overestimated and underestimated depending on the field strength (Figure 11 and Figure 12). The resulting values from the 1.5 T acquisitions are 17.4/2.14/0.41 which is comparable to literature values. The 3 and 7 T acquisitions, however, are somewhat overestimated and underestimated, respectively.

Since the estimated data in this work only reflects one volunteer, the deviations from literature values could be due to individual variations and not because of the method of choice. In the future, data from more than one volunteer should be considered to minimize individual variations.

The estimations of *cl* and *ndb* using spectroscopy at 1.5 T shown in Figure 12 are greatly overestimated compared to the estimations using the imaging data, estimations performed using 3 and 7 T acquisitions, and values obtained from the references mentioned above. This could be caused by difficulties estimating peak amplitudes and calculating T_2 relaxations

times due to low spectral resolution in the acquired spectrum. The estimation of the diacyl resonance, which is an important peak in the estimation of *cl, ndb* and *nmidb,* was particularly difficult because of, sometimes, undetectable amplitude. The T_2 relaxation time of the methylene resonance was used as the T_2 relaxation time of the peaks with incalculable T_2 relaxation values.

Even though the trends between the parameters (*cl* and *ndb*, *nmidb* and *ndb*) do not match the trends found using data acquired at 3 T by Bydder well, the diagrams in Figure 13 suggest some dependence on *ndb*. Especially the dependence of *cl* to *ndb* at 1.5 and 3 T seems to differ from the trends suggested by Bydder. If relationships between the parameters do exists, only the estimation of *ndb* would be needed and a more robust algorithm could be obtained. To determine these possible relationships, additional investigations are, however, needed.

Comparing the general performance of the MRI method with MRS, there are some advantages in terms of work load and convenience. Evaluation of spectrum data in a number of locations is more time consuming compared to imaging and require an experienced observer. Although development of reconstruction of MRI data requires expertise, the finished algorithm should increase evaluation objectiveness and automation compared to MRS. Apart from the spatial information gained with MRI, it also gives the viewer a more intuitive overview of the fat content and FA composition. In clinical use, it may be more convenient to use standardized values of T_2 relaxation times and chemical shifts in the MRI method instead of performing MRS on every patient. The potential errors introduced by using standardized values needs to be investigated further.

7. Conclusions

Despite problems with increased field inhomogeneity at higher field strengths, the results indicate improvement in accuracy when quantifying fat content and FA composition, both in vivo and in phantom, using the investigated MRI method at higher field strengths. This needs to be investigated further.

Comparing the accuracy of the MRI with the MRS method, the image-based method was equally good (if not better) in this study.

In this work and using these MRI parameter settings, it was found that approximately twenty echoes was a good choice for reconstruction.

The images acquired using the larger matrix size resulted in a noisier reconstruced image and a slightly different estimation of *ndb*. The estimation of *FF* is somewhat overestimated and the estimation of *ndb* is less accurate when using a larger flip angle. Consequently, no advantage in using a large flip angle was found. The impact of using a lager matrix size needs to be investigated more.

By analysing data acquired at 3T, Bydder et al. suggests empirical relationships of *ndb*, *nmidb* and *cl*, which did not match the in vivo results obtained in this work perfectly, although the results show a trend. This indicates the possibility of estimation only *ndb* as a quantification method and therefore a possibility of a more robust method. However, additional research is needed.

8. Acknowledgements

References

1.	Araya, J., R. Rodrigo, L.A. Videla, L. Thielemann, M. Orellana, P. Pettinelli, and J. Poniachik, *Increase in long-chain polyunsaturated fatty acid n - 6/n - 3 ratio in relation to hepatic steatosis in patients with non-alcoholic fatty liver disease.* Clin Sci (Lond), 2004. **106**(6): p. 635-43.

2.	Puri, P., R.A. Baillie, M.M. Wiest, F. Mirshahi, J. Choudhury, O. Cheung, C. Sargeant, M.J. Contos, and A.J. Sanyal, *A lipidomic analysis of nonalcoholic fatty liver disease.* Hepatology, 2007. **46**(4): p. 1081-90.

3.	Riserus, U., W.C. Willett, and F.B. Hu, *Dietary fats and prevention of type 2 diabetes.* Prog Lipid Res, 2009. **48**(1): p. 44-51.

4.	Dixon, W.T., *Simple proton spectroscopic imaging.* Radiology, 1984. **153**(1): p. 189-94.

5.	Reeder, S.B., Z. Wen, H. Yu, A.R. Pineda, G.E. Gold, M. Markl, and N.J. Pelc, *Multicoil Dixon chemical species separation with an iterative least-squares estimation method.* Magn Reson Med, 2004. **51**(1): p. 35-45.

6.	Yu, H., A. Shimakawa, C.A. McKenzie, E. Brodsky, J.H. Brittain, and S.B. Reeder, *Multiecho water-fat separation and simultaneous R2* estimation with multifrequency fat spectrum modeling.* Magn Reson Med, 2008. **60**(5): p. 1122-34.

7.	Hu, H.H., K.S. Nayak, and M.I. Goran, *Assessment of abdominal adipose tissue and organ fat content by magnetic resonance imaging.* Obes Rev, 2011. **12**(5): p. e504-15.

8.   Yu, H., C.A. McKenzie, A. Shimakawa, A.T. Vu, A.C. Brau, P.J. Beatty, A.R. Pineda, J.H. Brittain, and S.B. Reeder, *Multiecho reconstruction for simultaneous water-fat decomposition and T2* estimation.* J Magn Reson Imaging, 2007. **26**(4): p. 1153-61.

9.   Griffitts, J., Y. Tesiram, G.E. Reid, D. Saunders, R.A. Floyd, and R.A. Towner, *In vivo MRS assessment of altered fatty acyl unsaturation in liver tumor formation of a TGF alpha/c-myc transgenic mouse model.* J Lipid Res, 2009. **50**(4): p. 611-22.

10.   Guillén, M.D. and A. Ruiz, *1H nuclear magnetic resonance as a fast tool for determining the composition of acyl chains in acylglycerol mixtures.* European Journal of Lipid Science and Technology, 2003. **105**(9): p. 502-507.

11.   Hamilton, G., D.L. Smith, Jr., M. Bydder, K.S. Nayak, and H.H. Hu, *MR properties of brown and white adipose tissues.* J Magn Reson Imaging, 2011. **34**(2): p. 468-73.

12.   Machann, J., N. Stefan, C. Schabel, E. Schleicher, A. Fritsche, C. Wurslin, H.U. Haring, C.D. Claussen, and F. Schick, *Fraction of unsaturated fatty acids in visceral adipose tissue (VAT) is lower in subjects with high total VAT volume - a combined 1 H MRS and volumetric MRI study in male subjects.* NMR Biomed, 2013. **26**(2): p. 232-6.

13.   Hamilton, G., T. Yokoo, M. Bydder, I. Cruite, M.E. Schroeder, C.B. Sirlin, and M.S. Middleton, *In vivo characterization of the liver fat (1)H MR spectrum.* NMR Biomed, 2011. **24**(7): p. 784-90.

14.   Johnson, N.A., D.W. Walton, T. Sachinwalla, C.H. Thompson, K. Smith, P.A. Ruell, S.R. Stannard, and J. George, *Noninvasive assessment of hepatic lipid composition: Advancing understanding and management of fatty liver disorders.* Hepatology, 2008. **47**(5): p. 1513-23.

15.   Lundbom, J., A. Hakkarainen, B. Fielding, S. Soderlund, J. Westerbacka, M.R. Taskinen, and N. Lundbom, *Characterizing human adipose tissue lipids by long echo time 1H-MRS in vivo at 1.5 Tesla: validation by gas chromatography.* NMR Biomed, 2010. **23**(5): p. 466-72.

16.   Peterson, P. and S. Mansson, *Simultaneous quantification of fat content and fatty acid composition using MR imaging.* Magn Reson Med, 2013. **69**(3): p. 688-97.

17.   Bydder, M., O. Girard, and G. Hamilton, *Mapping the double bonds in triglycerides.* Magn Reson Imaging, 2011. **29**(8): p. 1041-6.

18.   Berglund, J., H. Ahlstrom, and J. Kullberg, *Model-based mapping of fat unsaturation and chain length by chemical shift imaging--phantom validation and in vivo feasibility.* Magn Reson Med, 2012. **68**(6): p. 1815-27.

19.   Ren, J., I. Dimitrov, A.D. Sherry, and C.R. Malloy, *Composition of adipose tissue and marrow fat in humans by 1H NMR at 7 Tesla.* J Lipid Res, 2008. **49**(9): p. 2055-62.

20.   Yu, H., A. Shimakawa, S.B. Reeder, C.A. McKenzie, and J.H. Brittain, *Magnitude Fitting Following Phase Sensitive Water-Fat Separation to Remove Effects of Phase Errors*, in *In: Proceedings of the 17th Scientific Meeting and Exhibition of the ISMRM*2009: Honolulu, Hawaii. p. 462.

21. Klose, U., *In vivo proton spectroscopy in presence of eddy currents.* Magn Reson Med, 1990. **14**(1): p. 26-30.

22. Nixon, T.W., S. McIntyre, D.L. Rothman, and R.A. de Graaf, *Compensation of gradient-induced magnetic field perturbations.* J Magn Reson, 2008. **192**(2): p. 209-17.